Applied Catalysis B: Environmental 176–177 (2015) 627–636

Contents lists available at ScienceDirect

Applied Catalysis B: Environmental

journal homepage: www.elsevier.com/locate/apcatb

Electrochemical oxidation of sour natural gas over $La_{0.4}Ce_{0.6}O_{1.8}$–$La_{0.4}Sr_{0.6}TiO_{3\pm\delta}$ anode in SOFC: A mechanism study of H_2S effects

Milad Roushanafshar[a], Ning Yan[a,b,**], Karl T. Chuang[a], Jing-Li Luo[a,*]

[a] Department of Chemical and Materials Engineering, University of Alberta, Edmonton, AB T6G 2V4, Canada
[b] Van't Hoff Institute for Molecular Sciences (HIMS), University of Amsterdam, Amsterdam 1098 XH, The Netherlands

ARTICLE INFO

Article history:
Received 12 November 2014
Received in revised form 18 April 2015
Accepted 22 April 2015
Available online 24 April 2015

Keywords:
Solid oxide fuel cells
Hydrogen sulfide (H_2S) effects
Methane (CH_4)
Electrochemical oxidation

ABSTRACT

For solid oxide fuel cell with $La_{0.4}Ce_{0.6}O_{1.8}$–$La_{0.4}Sr_{0.6}TiO_{3\pm\delta}$ (LDC-L4ST) impregnated anodes, the electrochemical oxidation rates of H_2 and CH_4 were significantly improved when H_2S (0.5%) was present in the feeds as evidenced by the substantially decreased polarization resistance and the improved power density of the cell although H_2S did not predominantly function as a fuel. Conductivity measurements of various anode component materials implied that the addition of H_2S into the feeds increased their conductivities. More importantly, from the mass spectroscopic analysis of the anode gas effluents and the thermodynamic calculations, direct evidences of H_2S caused SOFC performance improvement have been confirmed, three distinct regions for the electrochemical oxidation pathways of 0.5% H_2S–CH_4 vs. overpotential (η) were proposed to explain the effect. The chemisorbed S species, together with LDC-L4ST, behaved as an effective catalyst promoting CH_4 oxidations via COS and CS_2 intermediates. The addition of LDC in the anode enhanced this synergic effect and further increased CH_4 electrochemical conversion as well as coking resistance in comparison of the L4ST anode.

1. Introduction

Solid oxide fuel cells (SOFCs) provide higher energy conversion efficiency with environmentally friendly products when compared to conventional power generation systems based on combustion process [1]. Replacing pure H_2 with hydrocarbon fuels such as natural gas can extend the applications of SOFCs and make them more economically viable [2]. However, choosing appropriate anode materials for such applications then becomes a critical issue because of the required high electrocatalytic activity, coking resistance and hydrogen sulfide tolerance [3–7]. Nickel based anode materials showed high electrocatalytic activity for H_2 oxidation [8], but they cannot tolerate coking when light hydrocarbons fuel the cell [9,10]. The addition of alloying elements such as Cu or cerium oxide based materials improved the stability of the anode [11–15]. However, the presence of H_2S in the fuels, particularly the high level of H_2S impurities in sour (raw) natural gas, still remains as a challenge [16–22].

Using sour fuels containing high concentration H_2S is more economical due to the reduced purification cost of the fuels. In order to achieve this objective, replacing Ni based catalysts with other anode materials is necessary [23–25]. Ceramic based anode materials, $La_{0.8}Sr_{0.2}Cr_{0.5}Mn_{0.5}O_3$ (LSCM) or $Gd_{0.2}Ce_{0.8}O_{1.9}$ (GDC), showed reasonable electrochemical activities toward H_2 and CH_4 oxidations, but exhibited instability in high H_2S level fuels [26,27]. Strontium titanate based oxides with perovskite structure are viable anode materials for high concentrations H_2S containing fuels [28–33]. The experimental results showed that this material was chemically and electrochemically stable when exposed to high concentrations of H_2S. One of the main drawbacks of this anode material is the low activities toward the oxidation of fuels [34] compared with other anode materials including cermets and LSCM [35].

An interesting observation when using H_2S containing fuel was that in contrary to the commonly known sulfur poisoning effects that led to catalysts deactivation and fuel cell performance degradations, the high concentration H_2S (>0.5 vol%) could improve the electrochemical oxidation of the feedstock. This H_2S enhancement effects have been reported when $La_{0.4}Sr_{0.6}TiO_{3\pm\delta}$ (L4ST) and $La_{0.3}Sr_{0.7}VO_3$ were employed [28,29,36]. Although several hypotheses, e.g., formation of 2-D sulfides on catalyst surface, have been proposed to address the abnormal behaviors of SOFC, more questions remain to be answered including but not limited

* Corresponding author. Tel.: +1 780 492 2232; fax: +1 780 492 2882.
** Corresponding author at: Van't Hoff Institute for Molecular Sciences (HIMS), University of Amsterdam, Amsterdam 1098 XH, The Netherlands.
Tel.: +31 0 20 525 6468.
E-mail addresses: N.Yan@uva.nl (N. Yan), Jingli.Luo@ualberta.ca (J.-L. Luo).

http://dx.doi.org/10.1016/j.apcatb.2015.04.046
0926-3373/

to whether H_2S acts as the major fuel and whether the sulfides are oxidized when cells are deeply biased.

In this paper, we analyzed the effect of high concentration H_2S (0.5%) on the electrochemical oxidations of H_2 and CH_4 using $L_{0.4}Ce_{0.6}O_{1.8}$ (LDC)-L4ST as the anode materials for SOFCs. The effect of LDC addition on the electrochemical oxidation of CH_4 and the anode conductivity of the impregnated anode structures were also investigated.

2. Experimental

To prepare the porous yttria-stabilized zirconia (YSZ) electrode for subsequent infiltration, a mixture of YSZ (Tosoh) and graphite (40 wt%) powders were homogenized initially. Then a paste was prepared by mixing the powders with α-terpineol (Alfa Aesar) and isopropanol (volume ratio 2:1) as a solution containing 5 wt% poly(vinyl butyral-co-vinyl alcohol-co-vinyl acetate) (molecular weight = 70,000–1,00,000, Aldrich) (PVB) and 5 wt% ethyl cellulose (Aldrich). The paste was screen printed onto both sides of an YSZ electrolyte disk (300 μm thick, 25 mm in diameter) and then sintered at 1200 °C for 5 h to form a layer with ~70 vol.% open porosity.

L4ST precursor solution was prepared by dissolving titanium(IV) propoxide (98%, Aldrich) and triethanolamine (Aldrich) (molar ratio 1:4) into an aqueous solution containing the appropriate amounts of lanthanum(III) nitrate hexahydrate (99.999%, Aldrich) and strontium nitrate (Adrich). LDC precursor solution was prepared by dissolving stoichiometric amounts of lanthanum(III) nitrate hexahydrate, ammonium cerium(IV) nitrate (99.99%, Aldrich) and glycine (Aldrich) into de-ionized water. The total metal ion concentrations in these solutions were 0.5 mol L^{-1}. The porous YSZ was impregnated with L4ST and LDC solutions sequentially. The impregnated solutions were decomposed at 400 °C following each impregnation step, and the final materials were calcined at 900 °C for 2 h. L4ST was impregnated four times to form electrodes having 16 wt.% deposits. LDC-L4ST sample was prepared by impregnation of LDC twice (10 wt.%) before L4ST (16 wt.%). The cathode electrode was prepared by co-impregnation of $Gd_{0.2}Ce_{0.8}O_2$ (GDC) and $La_{0.6}Sr_{0.4}Co_{0.2}Fe_{0.8}O_3$ (LSCF) into the porous electrode of the opposed side of the electrolyte. GDC precursor aqueous solution (0.5 mol L^{-1}) was prepared by dissolving gadolinium(III) nitrate hexahydrate (99.9%, Aldrich), ammonium cerium(IV) nitrate and glycine in distilled water with 0.2:0.8:2 molar ratio. LSCF precursor solution was also prepared in the same way by using appropriate amounts of lanthanum(III) nitrate hexahydrate, strontium nitrate, cobalt(II) nitrate hexahydrate (98+%, Aldrich) and iron(III) nitrate nonahydrate (Aldrich). GDC preparation solution was impregnated twice (10 wt.%), then decomposed at 400 °C after each impregnation, followed by the calcination at 900 °C for 2 h. Then, LSCF solution was impregnated four times (16 wt.%) using the same decomposition and calcination sequence. Similarly, symmetrical cells were prepared by impregnating the same electrode materials into porous layers at both sides of the electrolyte. The cells were fixed onto a ceramic fixture and inserted into a quartz tube which was placed into the furnace. Humidified feed with 3 vol.% H_2O was used as the feed for the anode of the symmetrical cell at temperatures between 800 °C and 900 °C.

After fuel cell membrane electrode assemblies (MEA) were prepared by infiltration, gold paste was applied onto both electrode surfaces to form the current collectors. The cells were affixed onto one end of the alumina tube, forming the outside wall of the anode compartment, then sealed with a glass sealant (Armcoseal 617), and placed into the furnace to cure the sealant in situ. H_2, CH_4, H_2S (0.5%)-H_2 and H_2S (0.5%)–CH_4 with the flow rate of 50 mL min^{-1} flowed through a water bubbler before going to the anode compartment while the cathode electrode was open to the ambient air. The operating temperature varied between 800 °C and 900 °C. Electrochemical analyses of the cells were performed using Solartron SI 1287 electrochemical interface equipped with SI 1260 impedance/ Gain-phase analyzer and a 4-probe configuration was applied (Fig. 1). I–V curves were measured with the two probes, WE (working electrode) and RF2 (reference electrode), attached to the anode and the other two, RF1 and CE (counter electrode), attached to the cathode. The stability tests were performed under galvanostatic condition (40 mA cm^{-2}) with two probes connected to the anode, one probe (CE) attached to the cathode and another probe (RF1) connected to Pt wire attached to the rim of the YSZ electrolyte disk as shown in Fig. 1. The exhaust of the anode tube was guided to a mass spectrometer (Pfeiffer Thermostar GSD 301) to be analyzed for the gas composition of the cell effluent. Microstructure of the electrodes of SOFCs was characterized using field emission scanning electron microscope (FE-SEM, JOEL 6301F) and a transmission electron microscopy (TEM) with a JEOL-JEM 2100 microscope. A Rigaku Geigerflex X-ray diffractometer (XRD) system was used to determine the phases of samples. For surface chemistry studies, X-ray photoelectron spectroscopy (XPS) was performed using a Kratos Analytical AXIS 165. An ION-TOF IV Time-of-Flight secondary ion mass spectrometer (ToF-SIMS) was used to examine the depth profile of the sample disks.

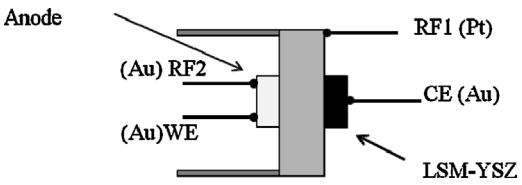

Fig. 1. A schematic of the 4-electrode configuration cell.

Four-point conductivity measurement technique was used for measuring the conductivity of the impregnated porous YSZ structure. Porous YSZ matrix bars (ℓ = 10 mm, d = 4.3 mm) were impregnated with different solutions to prepare LDC, L4ST and LDC-L4ST containing structures, which were then calcined to form the desired phase. Two probes were adjusted in the middle of the bar with a fixed distance (5.5 mm) to measure the potential difference along the bar. Two other probes were fixed onto both ends of the bar, providing current into the bar. Gold paste and gold wires were used as the current collectors. The potential differences between the potential probes were measured at different applied current using 0.2 mA, 0.4 mA, 1 mA as well as reverse polarities using −0.2 mA, −0.4 mA and −1 mA under galvanoastatic conditions. The resistances of samples were measured in different atmospheres including air, H_2 and H_2S (0.5%)-H_2 between 700 °C to 900 °C using the slope of the potential-current line. The specific electrical conductivities of the samples were calculated using Eq. (1):

$$\sigma = \frac{L}{R \times A} \quad (1)$$

where σ is the conductivity of the porous structure, L is the distance between the potential probes, A is the surface area of the bars and R is the measured resistance of the samples. Temperature programmed oxidation (TPO) method was used to analyze the carbon deposition on the anode materials. Two samples containing L4ST and LDC-L4ST anode materials were exposed to H_2S (0.5%)-CH_4 feed (50 mL min^{-1}) under 0.7 V potentiostatic run for 20 h at 800 °C. The feed was switched to N_2 under open circuit voltage (OCV) condition and cooled down to room temperature at 5 °C min^{-1}. Samples were put into a quartz tube connected to a mass spectrometer and oxidized using O_2 (10%)-He with the temperature ramping from room temperature to 1000 °C at 1 °C min^{-1} heating rate.

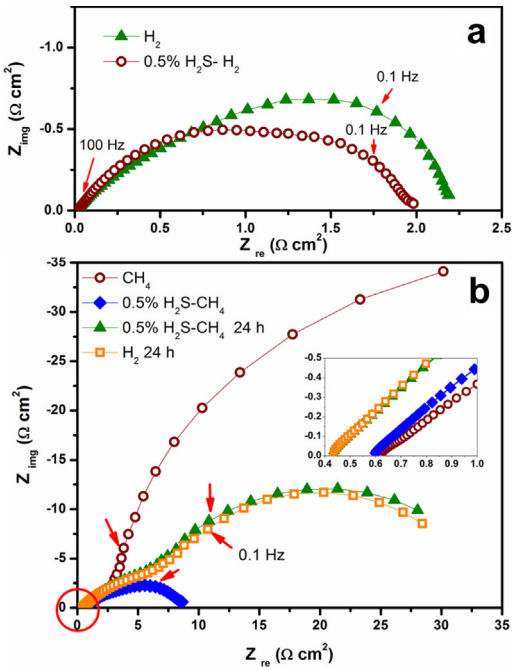

Fig. 2. EIS results under open circuit condition at 800 °C for symmetrical cell fueled by (a) H_2 or 0.5% H_2S–H_2; (b) with the sequence of CH_4, 0.5% H_2S–CH_4, 24 h in 0.5% H_2S–CH_4, and 24 h in H_2 after 24 h exposure in 0.5% H_2S–CH_4.

3. Results and discussions

3.1. Fuel cell performance enhancements in H_2S containing fuels

Fig. 2 compares EIS results for the symmetrical cell using LDC-L4ST anode material on both sides of the electrolyte in different fuels at 800 °C. The area specific polarization resistance (ASR_{pol}) of the anode decreased from 2.1 Ω cm^2 to 1.8 Ω cm^2 when H_2S (0.5%) was added into the H_2 feed, as shown in Fig. 2a. When CH_4 was purged into the cell, ASR_{pol} of the cell increased to 78.35 Ω cm^2 since methane molecules were more difficult to be activated by the catalyst (Fig. 2b). Similarly, when the gas was switched from CH_4 to 0.5% H_2S–CH_4, ASR_{pol} drastically dropped to 8.6 Ω cm^2. However, after 24 h exposure to the sour natural gas environment, ASR_{pol} increased to 34.8 Ω cm^2 and remained constant during 24 h exposure. This change was irreversible after switching to H_2 feed stream. In consideration of the relatively stable and low ASR_{pol} in 0.5% H_2S–H_2 in Fig. 2a, it was concluded that anode sulfur poisoning or sulfidation was unlikely to cause such increase. Because CH_4 can thermally decompose or be reformed by either H_2O or H_2S, producing carbon species on the anode at the experimental conditions, carbon deposition, which could not be easily removed under OCV condition when the cell was not biased, could be the reason for the electrochemical performance degradation. This conjecture was supported by the decreased ohmic resistances resulting from carbon deposition after 24 h operations as shown in the inset of Fig. 2b.

In Fig. 3a, the SEM image of LDC-L4ST infiltrated anode after fuel cell test shows that the infiltrates were well-distributed across the entire YSZ matrix without forming segregates near the surface. The morphology analysis carried out by TEM demonstrated that all YSZ particles had been fully covered by LDC-L4ST (Figs. 3b and c). Fig. 4 compares the power densities of the cell when H_2 and 0.5% H_2S-H_2 fed the anode at 900 °C. The peak power densities of the cell were improved from 161 mW cm^{-2} to 256 mW cm^{-2} when H_2S was added into the feed. Fig. 5 illustrates the effect of H_2S addition on the power density of the cell when CH_4 fueled the cell at 900 °C. The peak power densities of 27 mW cm^{-2} and 158 mW cm^{-2} were obtained when CH_4 and 0.5% H_2S–CH_4, respectively, fueled the cell. It is interesting to have observed that the OCV of SOFC in H_2S-containing fuels seems to be higher than the theoretical Nernst

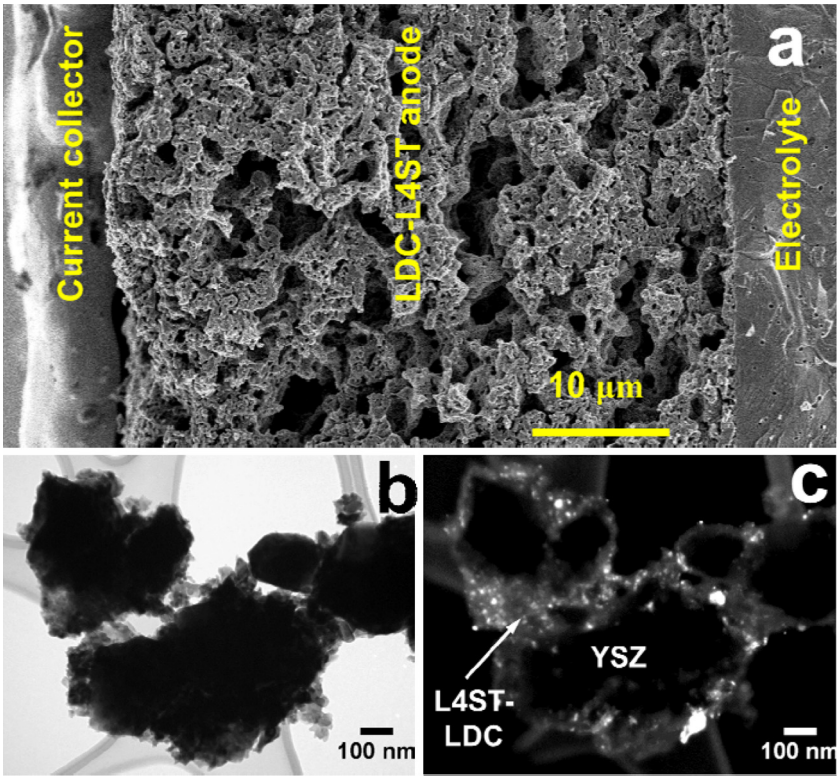

Fig. 3. (a) A SEM image of LDC-L4ST infiltrated anode after fuel cell test; (b) bright field and (c) dark field TEM images of LDC-L4ST infiltrated YSZ anode materials.

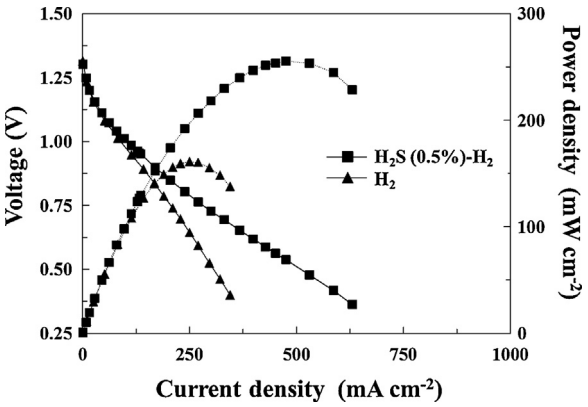

Fig. 4. Polarization and power density vs. current density curves when H_2 and 0.5% H_2S–H_2 fuelled the cell at 900 °C.

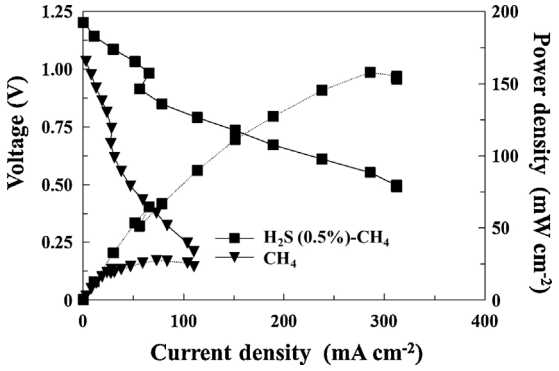

Fig. 5. Polarization and power density curves when CH_4 and 0.5% H_2S–CH_4 fuelled the anode at 900 °C.

Table 1
Peak power densities of SOFC with different anode materials in various fuels at 800 °C.

	Peak power densities (mW cm^{-2})			
	H_2	H_2S (0.5%)–H_2	CH_4	H_2S (0.5%)–CH_4
L4ST	20	36	3	30
LDC	50	52	6	30
LDC-L4ST	76	110	7	75

potential in the corresponding pure fuels, this scenario has been found in the previous work and was ascribed to the contaminants of sulfur compounds [28]. Table 1 compares the peak power densities of the cells with different anode materials when different feeds fueled the cells. It can be seen that the fuel cell performances were greatly enhanced when H_2S was present in the feed stream, with only one exception from using pure LDC as the anode, probably due to the formation of Ce_2O_2S [37,38]. However, the addition of H_2S improved the electrochemical oxidation of CH_4 regardless of the anode material. Additionally, LDC-L4ST composite anode had the best performance as a result of the combination of high electronic conductivity from L4ST and improved activity from LDC.

In fact, H_2S was commonly considered as a strong poisoning agent that can deactivate most of the anode catalysts [16–22], e.g., Ni and CeO_2. The observed fuel cell performance enhancements when high concentration of H_2S was present were widely documented in the literature [28,29]. However, no consensus had been reached in explaining this abnormal behavior of fuel cells. Because numerous reports have proved the crystalline stability of $(La,Sr)TiO_3$ in the relevant H_2S environments [28], we hereby examined the contribution of H_2S conversion toward fuel cells performances, the influences of H_2S over the electrical properties of the anode, and the synergic effects of H_2S-catalysts over fuel electrochemical oxidation.

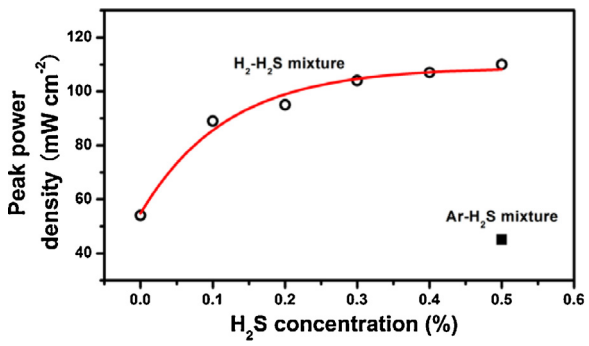

Fig. 6. Peak power density variations as a function of H_2S concentrations when H_2 or Ar fed the anode compartment of the cell at 800 °C.

3.2. H_2S as the major fuel?

The most straightforward hypothetic explanation of H_2S enhancement effects was the significant contribution of the electrochemical oxidation of H_2S to the promoted fuel cell power densities. Thus, variations of peak power densities as a function of H_2S concentrations at 800 °C were monitored as shown in Fig. 6. The addition of 0.1% H_2S into H_2 fuel improved the power density of the cell from 54 mW cm^{-2} to 89 mW cm^{-2}. Further addition of H_2S to 0.3% slightly improved the peak power density to 105 mW cm^{-2}. From that point on, there were no significant variations when H_2S concentration was increased to higher levels and a plateau of peak power density had been reached. In contrast, when the balance gas was switched from H_2 to Ar that is inert, the maximum power density was merely 45 mW cm^{-2} in 0.5% H_2S + Ar. This proved that H_2S alone was unlikely the main reason for inducing the dramatic promotion of fuel cell performance despite the fact that it indeed contributed to the electrochemical current. H_2 was still the major source of fuels in the cell. This conclusion was also supported by the mass spectrometric data obtained from anode effluents, which will be discussed in details in the following sections.

Similar to H_2O molecule, H_2S is also able to reform CH_4 molecule that is relatively more stable at elevated temperatures, leading to the formation of various derivatives, e.g., H_2, which are easier to be activated by electrocatalysts. This H_2S-assisted CH_4 reforming effect was also taken into account when exploring the fuel cell performance enhancement in H_2S–CH_4. Table 2 shows the equilibrium compositions (calculated via software HSC Chemistry 5.1 at 800 °C) of natural gas with different original compositions. The molar quantities of original gas species were determined in accordance with fuel compositions applied in SOFC test. It can be found from the table that 3 mol of H_2O in 99.5 mol of CH_4 can lead to the formation of 9 mol of H_2 and 3 mol of CO at the equilibrium state. In contrast, 0.5 mol of H_2S is a much weaker reforming agent that is capable of generating only 0.99 mol of H_2 or 0.61 mol of extra H_2 when H_2O is present. Meanwhile, it can also cause the formation of CS_2 though the quantity of which is too low to improve fuel cell performance significantly. Therefore, it is rational to conclude that H_2S-assisted CH_4 reforming was unlikely to induce remarkable power increase of SOFC either.

3.3. Electrical properties change in H_2S-containing fuels?

It was also of great interest to examine if the presence of H_2S altered the electrical properties of the anode materials, i.e., the increased conductivity of the anode in H_2S containing atmosphere

Table 2
Equilibrium compositions at 800 °C of H_2O and/or H_2S containing CH_4.

Original Composition (mol)	Equilibrium composition (mol)							
	CH_4	H_2	CO	H_2S	CS_2	COS	H_2O	CO_2
CH_4 (99.5) + H_2O (3)	96.5	9.00	3.00	N/A	N/A	N/A	1.37×10^{-5}	4.92×10^{-6}
CH_4 (99.5) + H_2S (0.5)	99.3	0.99	N/A	2.86×10^{-3}	0.25	N/A	N/A	N/A
CH_4 (99.5) + H_2S (0.5) + H_2O (3)	96.3	9.61	3.00	0.20	0.15	2.73×10^{-3}	1.64×10^{-5}	5.53×10^{-6}

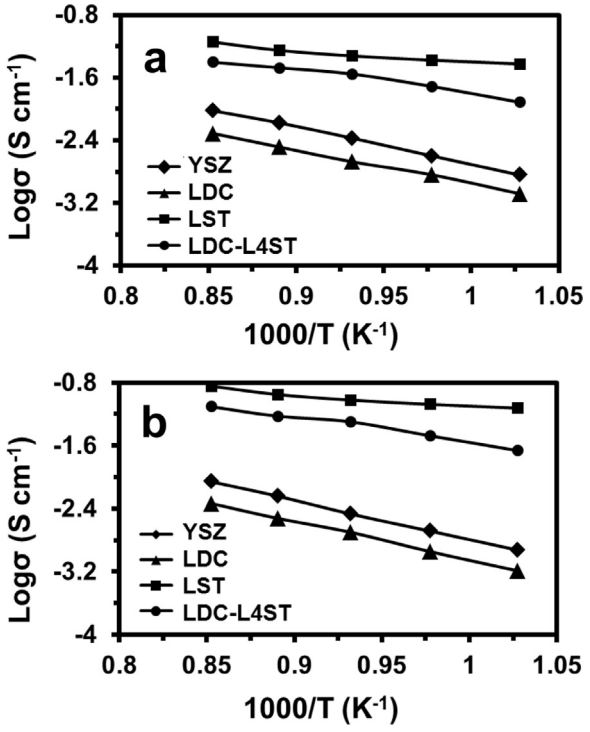

Fig. 7. 4-point conductivity measurement results for YSZ, LDC, L4ST and LDC-L4ST samples in (a) H_2, (b) 0.5% H_2S–H_2, at different temperatures between 700 °C and 900 °C.

could reduce the ohmic loss and therefore, improve the performance of the cell. Accordingly, conductivity (σ) measurements were carried out in various environments as shown in Fig. 7. Fig. 7a compares the conductivities of materials in pure H_2 atmosphere. The results showed that the total conductivity of the porous YSZ in H_2 was ~0.01 S cm^{-1}. The conductivity of the LDC impregnated porous YSZ was reduced to 0.005 S cm^{-1}, which was attributable to the high resistivity of the loosely packed LDC deposits on the YSZ surface. The L4ST containing sample was the most conductive one in reducing environment with the conductivity of 0.07 S cm^{-1} at 900 °C. The same improvement was also observed for LDC-L4ST infiltrated sample, with a conductivity of 0.04 S cm^{-1} in H_2 at 900 °C. In fact, L4ST has low ionic conductivity when compared with other ion conductive materials including YSZ, Mg doped (La,Sr)GaO_3 and ceria based materials [39–41]. The high conductivity was largely due to the low electronic resistivity. It is an *n*-type semiconductor with higher conductivity in reducing atmosphere because of the reduction of Ti^{4+} cation to Ti^{3+}, leaving electrons in the conduction band.

In comparison, Fig. 7b shows the total conductivities of YSZ structure, LDC, L4ST and LDC-L4ST impregnated structures after exposure to 0.5% H_2S-H_2. The conductivity of the blank YSZ matrix was similar to that in H_2, with the value of 0.01 S cm^{-1}, indicating that H_2S did not affect the conductivity of YSZ. The conductivity of LDC impregnated porous YSZ remained constant after adding H_2S into the environment. However, the total conductivities of the L4ST-containing materials were improved approximately twice in the presence of H_2S with 0.14 S cm^{-1} for L4ST and 0.078 S cm^{-1} for LDC-L4ST samples at 900 °C. Since the presence of 0.5% H_2S did not change the crystalline structure of L4ST [28], the surface chemistry alternation, e.g., dissociative adsorption of H_2S on L4ST, could be the key for such a conductivity improvement. An analogous scenario was reported in which 3% of H_2S interacted with TiO_2 and changed its conductivities in several steps [42]. Since L4ST is an n-type semiconductor, its electronic conductivity can be enhanced by donated electrons from electron donors such as H_2S into its conduction bands. It could also be possible that a modification of the surface chemistry of the titanate occurred due to the adsorbed S species. The replacement of O^{2-} by S^{2-} on the surface of the L4ST and the subsequent redox property change might also be one of the reasons [42]. However, it is obvious that more work needs to be done to fully understand the origin of the conductivity difference in the presence of H_2S.

3.4. H_2S as the promoter of electrochemical reactions?

H_2S has been reported to be able to modify the catalytic properties of a wide spectrum of catalysts [26–33]. In this section, its influences over the catalytic conversion of CH_4 on LDC-L4ST were investigated in details. Fig. 8a shows the mass spectroscopic signals of various species from anode effluent as a function of fuel cells overpotential (η) when 0.5% H_2S–CH_4 fueled the cell. Generally, CH_4 consumption did not commence till η was higher than 0.2 V (when OCV = 1.17 V, η = 0 V). Interestingly, its electrochemical conversion was not enhanced further in accordance with the increasing fuel cell current when η was higher than 0.5 V. This trend was also followed by signals of H_2O and CO_2 and confirmed by the backward polarization curve at the corresponding voltage in Fig. 8b. Meanwhile, it should be noted that the signal of CO was maintained at constant without any noticeable variations, indicating that CO might not be the intermediate of CH_4 oxidation and the direct electro-oxidation of CH_4 likely occurred in the fuel cells.

Sulfur-containing compounds were another major gas species in the feed. The result showed that the level of H_2S, without being oxidized, was almost constant till the polarization voltages dropped to lower than 0.5 V. SO_2 production and H_2S consumption occurred after 0.5 V of polarization, the same potential with the maximum of CO_2/H_2O signals and the cease of CH_4 conversion increase. This scenario provided direct evidences that H_2S has played a vital role in CH_4 electro-oxidation in SOFC. To predict the possible reaction pathways/mechanisms as well as the roles of H_2S in the catalytic processes in according with the observations, the polarization curve has been categorized into three regions with details discussed in the following sections. The most relevant reactions are listed in Table 3.

Region I is defined as $\eta = 0 \sim 0.2$ V. At SOFC operating temperature, a number of reactions could occur spontaneously in the CH_4-H_2S gas mixture (the equilibrium composition is shown in Table 1) including R1 ~ R3 listed in Table 2. Consequently, the surface of the catalyst was covered with sulfur and carbon species which were ready to react. R4 ~ R8 compares the change of Gibbs free energy (ΔG) for the possible oxidation reactions when cell was biased. Apparently, after the surface carbon was oxidized through

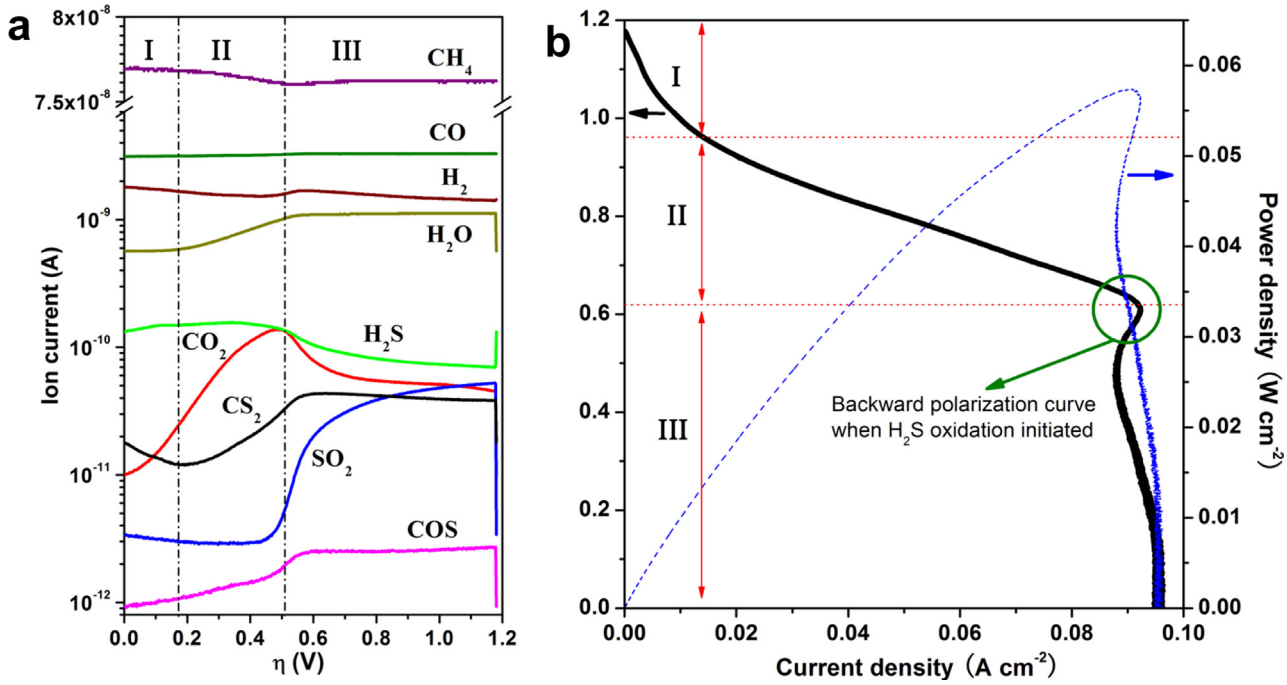

Fig. 8. (a) Mass spectroscopic signals of various species from anode effluent as a function of fuel cells overpotential and (b) the corresponding polarization and power density curves, when 0.5% H_2S–CH_4 fuelled the cell employed with LDC-L4ST anode at 800 °C. The potential scan rate was 0.2 mV s^{-1}.

R6, releasing more active sites for the electrochemical reactions, conversion of CS_2 (R4 and R5) became thermodynamically more favorable than either R7 or R8 when oxygen flux was fixed. Therefore, the concentration of CS_2 would decrease, and only COS and CO_2 signals in the MS would increase whereas those for H_2O and H_2S would remain constant when oxygen ions were supplied at low overpotential conditions, i.e., at low pO_2, CS_2 was preferentially converted in the anode chamber while H_2, CH_4 or H_2S remained unreacted. From the perspective of catalytic process, CS_2 was an easily activated species by titanate catalyst in a SOFC. Vincent et al. [28] reported that for SOFC fed by diluted CS_2 balanced with argon, the resulting peak power density was around 6 mW cm^{-2} at 850 °C when CS_2 concentration was only 200 ppm. Hence, it is not a surprise to observe preferential oxidation of CS_2 in this polarization region.

Region II is defined as $\eta = 0.2 \sim 0.5$ V. After region I processes, carbon deposits on the anode prior to cell polarization had been converted considerably. Thus, in this region, when η was higher than 0.2 V, there were more active sites available as well as higher pO_2 to facilitate CH_4 oxidation [43]. Usually, CH_4 would approach

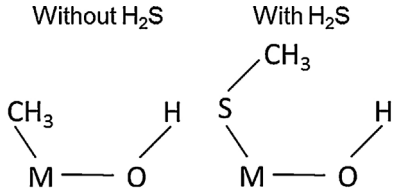

Fig. 9. Possible activation process of CH_4 on metal oxide (M = Ti and Ce).

the transition metal oxide with its methyl group ($-CH_3$) attacking the metal [44]. When H_2S was dissociatively adsorbed on the same catalyst, the formed sulfur atoms also mainly interacted with the metal centers of the surface [45,46]. Because H_2S is a dipole molecule with strong interaction with catalysts, the majority of metal centers on the surface would be occupied by S species. Therefore, in the H_2S–CH_4 mixture, CH_4 would actually interact with these S atoms, forming —S—CH_x intermediates. This process, shown in Fig. 9 assuming a-top adsorption dominated [45], might be thermodynamically and/or kinetically more favorable than direct

Table 3
Possible chemical and electrochemical reactions within SOFC fed by 0.5% H_2S–CH_4.

No.	Reactions[a]	ΔG_0[800 °C] (kJ mol^{-1})
R1	$CH_4(g) + 2H_2S(g) \leftrightarrow CS_2(g) + 4H_2(g)$	[b]
R2	$CH_4(g) \leftrightarrow C + 2H_2(g)$	[b]
R3	$2H_2S(g) \leftrightarrow 2H_2(g) + S_2(g)$	[b]
R4	$CS_2(g) + O^{2-} \leftrightarrow COS(g) + 1/2S_2(g) + 2e^-$	−199.16
R5	$1/2CS_2(g) + O^{2-} \leftrightarrow 1/2CO_2(g) + 1/2S_2(g) + 2e^-$	−189.07
R6	$1/2C + O^{2-} \leftrightarrow 1/2CO_2(g) + 2e^-$	−197.97
R7	$H_2(g) + O^{2-} \leftrightarrow H_2O(g) + 2e^-$	−188.69
R8	$H_2S(g) + O^{2-} \leftrightarrow 1/2S_2(g) + H_2O(g) + 2e^-$	−151.12
R9	$CH_4(g) + 4O^{2-} \leftrightarrow CO_2(g) + 2H_2O(g) + 8e^-$	−800.46
R10	$CH_{x[ad]} + S_2(g) \leftrightarrow CS_2(g) + xH_{[ad]}$	
R11	$CS_{[ad]} + O^{2-} \leftrightarrow COS + 2e^-$	
R12	$H_2S(g) + 3O^{2-}(g) \leftrightarrow SO_2(g) + H_2O(g) + 6e^-$	−434.695
R13	$S_2(g) + 4O^{2-}(g) \leftrightarrow 2SO_2(g) + 8e^-$	−567.15

[a] Thermodynamic data of $O_2(g)$ were used.
[b] $C_{reactants} \gg C_{products}$ making ΔG_0 not a good reference in predicting reaction directions.

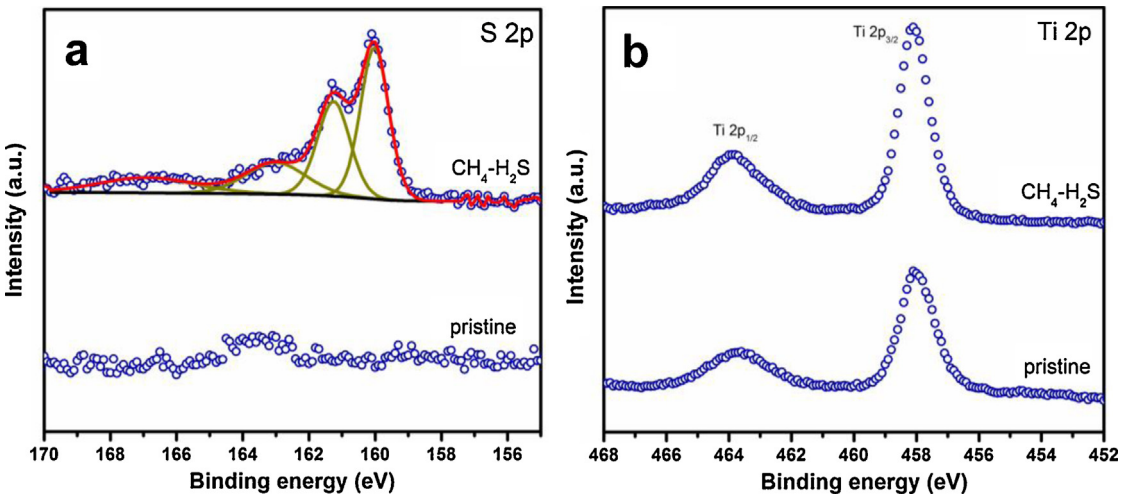

Fig. 10. XPS spectra of pristine and H_2S treated L4ST samples: (a) S 2p, and (b) Ti 2p spectra.

interaction of Ti with methyl groups, which required less activation energy.

In order to reveal the surface chemistry of the catalyst as well as to characterize the actual active sites, high resolution XPS analysis data are shown in Fig. 10. Compared with pristine L4ST with basically no sulfur signals, the spectrum of S 2p (Fig. 10a) on sour natural gas treated L4ST could be deconvoluted into four distinct peaks. The peak with a binding energy at ~160 eV was usually believed to be related to the chemisorbed sulfur or sulfides species. The adjacent peak at ~161.5 eV was assignable to the –SH groups whereas the peak at ~163 eV was due to the formation of sulfur deposits (physisorbed elemental sulfur). The wide but weak peak located between 166 and 168 eV was attributable to sulfate (SO_4^{2-}) or sulfite (SO_3^{2-}) species formed due to catalyst surface oxidations when exposed to the ambient air. The appearance of the spectrum did not change apparently when LDC was added to L4ST. Therefore, the active site proposed in Fig. 9 was confirmed to be chemisorbed S, –SH and elemental sulfur species. Fig. 10b compares Ti 2p spectrum before and after sour gas treatment, there was no noticeable peak shift or new peak formation, this result is in good agreement with the previous work in terms of titanate stability [28]. Fig. 11 demonstrates the ToF-SIMS depth profile of L4ST sample disc after exposure to sour gas. It is clear that the near-surface region had the concentrated sulfur species including S and –SH as shown by the two peaks indicated by the arrows in Fig. 11. After ~100 s of sputtering, the concentration of TiO fragment started to rise whereas that of S-containing counterpart tended to decrease and stabilize, implying the probe ion-beam had reached the L4ST matrix.

It could be seen from Fig. 8a that CH_4 consumption as well as H_2O production appeared and increased while that of CO_2 was continuously rising. Since more CH_4 molecules were activated, the adsorbed species ($CH_{x[ad]}$) could react with surface S through R10 to generate more CS_2, leading to the signal intensity increase of CS_2. In the meantime, a portion of surface – SC species was neither sufficiently "sulfurized" to form CS_2 nor completely oxidized to form CO_2, but partially oxidized to form COS though R11. However, there was still no SO_2 production occurring via R12 or R13 due to the inadequate pO_2 under this polarization conditions [47]. The catalyst surface was still likely to be covered by sulfur species.

Region III is when $\eta > 0.5$ V. In this last region, the SO_2 production suddenly occurred at $\eta = 0.5$ V and its signal intensity increased remarkably. Intensity of H_2S reduced instead, further implying the commencement of H_2S and/or S_2 electrochemical consumptions (R12 and R13). Normally, as the overpotential increased and an additional species started to participate in the electrochemical reactions, the fuel cell performance would be improved accordingly. However, in this region, the conversion of H_2S and/or S_2 resulted in a simultaneous large decrease of CO_2 concentration while no further CH4 oxidation or H_2O production occurred after reaching a plateau as η increased. Meanwhile, signals of other species also seemed to be steady, suggesting that the relevant processes had reached equilibriums. More surprisingly, in the polarization curve, when η increased from 0.5 V to ~1.2 V, the current did not increase all the times but started to drop coincidentally when H_2S consumption occurred (Fig. 8b). These observations suggested that there must be a strong interrelation between CH_4 oxidation and reduced sulfur species in the feed stream, the most presumable hypothesis was that the surface sulfur species had a synergic effect with LDC-L4ST, which promoted the electrochemical oxidation of CH_4.

Fig. 12 is a schematic of the electrochemical conversion mechanisms of fuels in three regions. In region I, conversions of carbon deposited at OCV conditions as well as CS_2 (the most easily oxidized species) predominated, producing CO_2 and COS. Because the cell was slightly biased, the current generated was very low. In region II, when the carbon removal left more active sites available on LDC-L4ST, H_2S would dissociatively adsorb on it while the level of pO_2 was still inadequate to oxidize those sulfur species (–S). A synergic effect between LDC-L4ST and —S was subsequently established, facilitating the activation and conversion of CH_4 by forming —S—CH_x and —SH at the adjacent active sites. These active species could then be fully oxidized into CO_2 and H_2O or partially

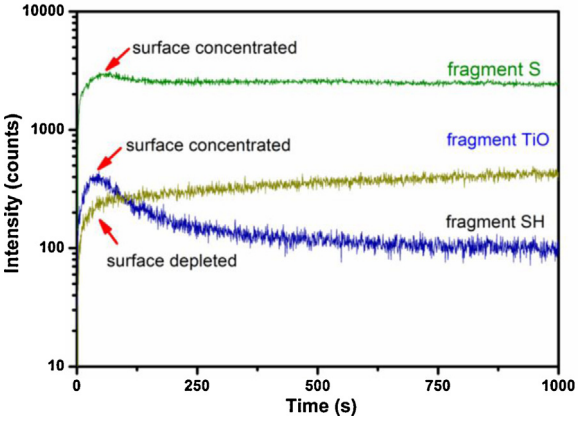

Fig. 11. ToF-SIMS depth profile of L4ST sample after treatment in 0.5% H_2S–CH_4.

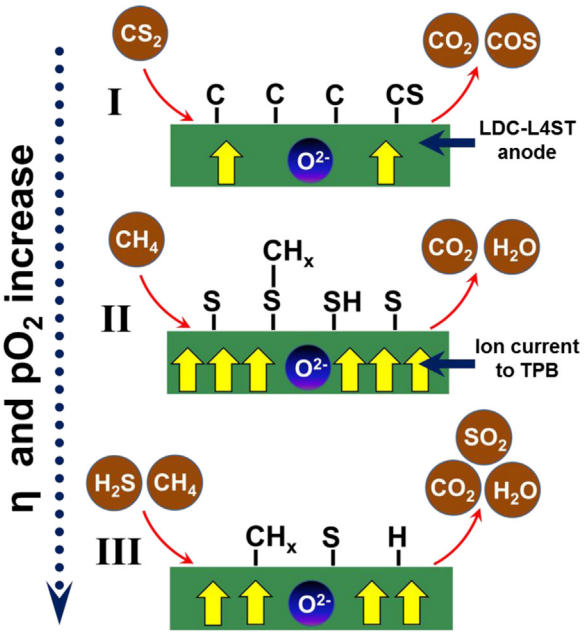

Fig. 12. A schematic of the electrochemical conversion mechanisms of fuels in three regions.

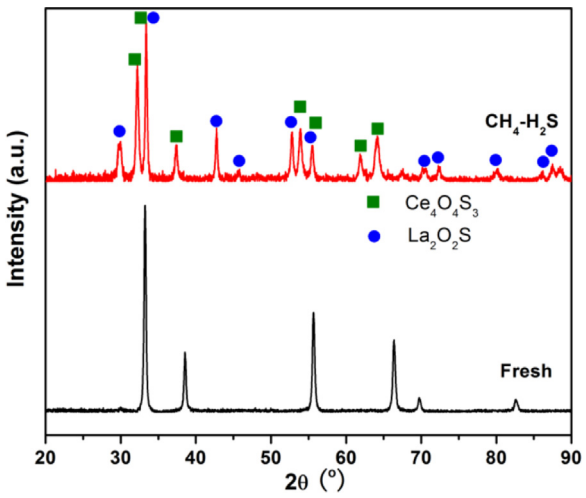

Fig. 14. XRD patterns of LDC before and after treatment in 0.5% H_2S–CH_4 at 800 °C for 24 h.

oxidized into COS. Due to the strong promotion effects, the fuel cell current increased and other performances improved significantly as well in this region where the direct CH_4 conversions took place. When η and pO_2 increased to enter region III, surface –S species was oxidized to produce SO_2. As the synergic effect was broken down due to either no —S species being available or no —S species at the adjacent active sites, CH_4 conversion catalyzed directly by LDC-L4ST prevailed and the current generated would in turn decrease as suggested by results from Fig. 8b.

3.5. Roles of LDC

At this point, it is understood that the higher conductivity of LDC-L4ST in H_2S environment and the synergic effect discussed above could optimize the SOFC performance in H_2S environments. The cell with LDC-L4ST anode was apparently better than that with pure L4ST. Thus, it was meaningful to have explored the functions of LDC.

Fig. 13 compares the different gas productions from the anode chamber of SOFCs when LDC-L4ST and L4ST were used as the anode materials, respectively. Note that the y axial was plotted linearly rather than logarithmically as shown in Fig. 8a. The general tendency was essentially identical in terms of the relationship between fuel oxidation and overpotential, suggesting H_2S, rather than LDC, remained the predominant effects. The H_2O production was similar for both cells, so were the signals of SO_2 and CS_2. However, the addition of LDC significantly promoted the conversion of CH_4 by producing much stronger CO_2 signals. Another finding was that for both LDC-L4ST and L4ST cells, they generally shared the same η at the inter-region boundaries. This agreed well with the previously discussed mechanisms in which the level of pO_2 was used as the criteria to determine the preferable reactions within the cell.

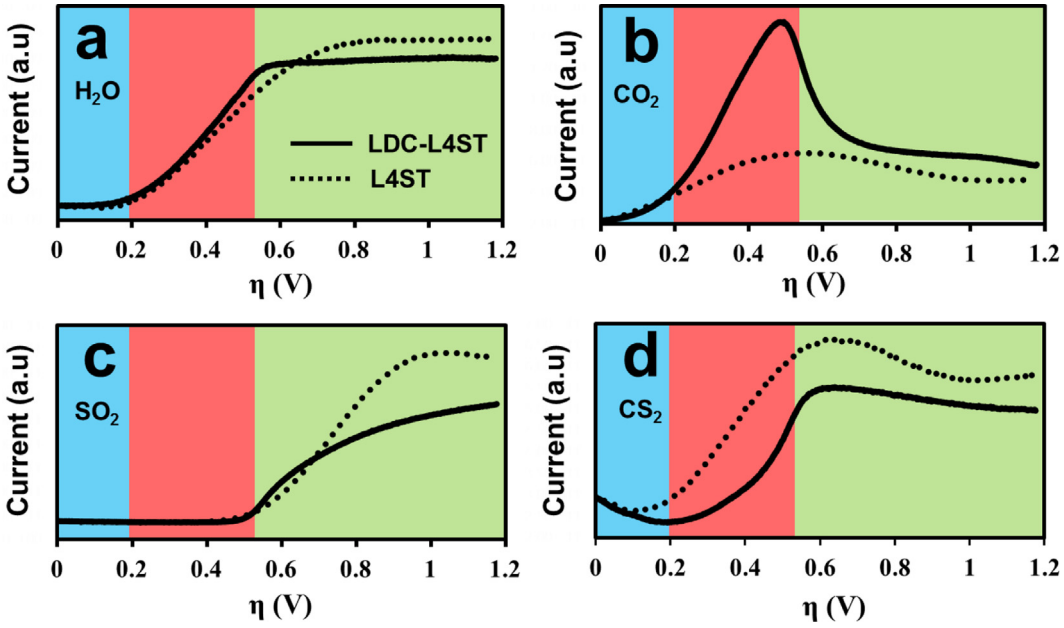

Fig. 13. Mass spectroscopy results of the outlet gas during potentiodynamic tests with 0.2 mV s^{-1} scan rate for: (a) H_2O, (b) CO_2, (c) SO_2, (d) CS_2 using L4ST and LDC-L4ST anode materials when 0.5% H_2S–CH_4 fuelled the cells at 800 °C.

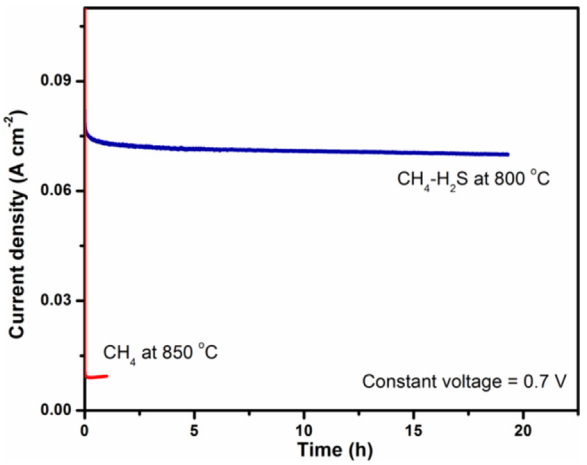

Fig. 15. Stability test of SOFC employed with LDC-L4ST anode under constant voltage (0.7 V).

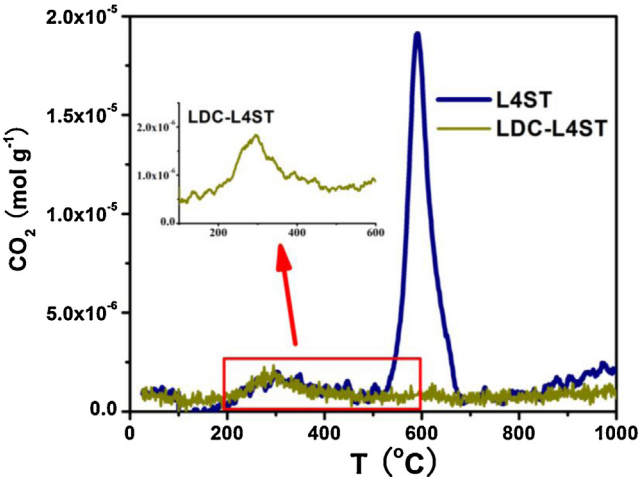

Fig. 16. TPO of the cells containing L4ST and LDC-L4ST anode materials after exposure to 0.5% H_2S–CH_4 under 0.7 V potentiostatic run at 800 °C for 20 h.

These results implied that LDC could enhance CH_4 electrochemical conversion, particularly in the second region. In fact, ceria based materials were well documented as the highly active catalysts toward the oxidation of hydrocarbons [48,49]. They also showed high affinity of H_2S via adsorption and the ability of forming oxysulfide phase [50,51]. Fig. 14 compares the XRD patterns of LDC before and after the treatment in CH_4–H_2S at 850 °C for 24 h. LDC has partially decomposed into $Ce_4O_4S_3$ and La_2O_2S which might have more active sulfur species on the surface, indicated by the higher S atomic ratio obtained from XPS analysis. That further improved the electrochemical oxidation of CH_4 through the synergic effect. The stability test result of SOFC employed with LDC-L4ST in 0.5% H_2S–CH_4 fuels for 20 h is shown in Fig. 15. The performance of the oxysulfide-L4ST composite catalyst did not degrade apparently within 20 h of test at 800 °C. In comparison, the fuel cell performance in pure CH_4 at 850 °C was also included in the figure, which was drastically lower than that in 0.5% H_2S–CH_4.

After operating both cells in 0.5% H_2S–CH_4 at 800 °C under 0.7 V constant load for 20 h, TPO was performed to evaluate the amount and types of the coke formed in the anode. From Fig. 16, it can be seen that within LDC-L4ST cell, there was only a small CO_2 peak at ~300 °C. The associated coke could be categorized as amorphous carbon and surface —S—CH_x species which were in presence as reaction intermediates on the catalyst surface, both of them could be readily removed by oxygen fluxes from the electrolyte. In contrast, for L4ST cell, in addition to the peak at ~300 °C, there was another much stronger CO_2 peak at ~600 °C. The corresponding carbon phase was believed to be the crystalline form of carbon, namely graphite. Because of the strong carbon-carbon bonds, graphite was unable to be removed easily by O^{2-}, it might accumulate at the triple-phase boundary (TPB) and slow down the subsequent conversion of CH_4. Alternatively, conclusions from TPO results also indicated that LDC did promote CH_4 oxidations.

4. Conclusions

LDC-L4ST anode was successfully fabricated by impregnation and demonstrated good performances toward 0.5% H_2S-containing H_2 and CH_4 oxidation in SOFC. The electrochemical tests revealed the effective roles of high concentrations H_2S in enhancing fuel cell performances, particularly when CH_4 fed the cell. This enhancement was not contributed by the oxidation of H_2S, but was significantly attributable to: (1) increased conductivity of LDC-L4ST in H_2S containing feed; (2) synergic effects of surface sulfur species with LDC-L4ST that facilitated CH_4 oxidation. A 3-region model based on the level of cell overpotential was proposed as the reactions pathways of H_2S-CH_4 electrochemical oxidations. The major function of L4ST in this composite anode was to increase the electronic conductivity whereas LDC was to increase the oxidation rate of CH_4 while prohibiting the formation of coke.

Acknowledgments

This research was supported through funding to the Natural Science and Engineering Research Council (NSERC) of Canada Strategic Grant and NSERC Solid Oxide Fuel Cell Canada Strategic Research Network. This work is also part of the Research Priority Area Sustainable Chemistry of the University of Amsterdam, The Netherlands, http://suschem.uva.nl.

References

[1] F. Alcaide, P.L. Cabot, E. Brillas, J. Power Sources 153 (2006) 47–60.
[2] K. Eguchi, H. Kojo, T. Takeguchi, R. Kikuchi, K. Sasaki, Solid State Ionics 152–153 (2002) 411–416.
[3] S.P. Jiang, S.H. Chan, J. Mater. Sci. 39 (2004) 4405–4439.
[4] T. Setoguchi, K. Okamoto, K. Eguchi, H. Arai, J. Electrochem. Soc. 139 (1992) 2875–2880.
[5] B.C.H. Steele, Solid State Ionics 86–88 (1996) 1223–1234.
[6] O. Marina, L. Pederson, in: J. Huijsmans, (Ed.) Fifth European Solid Oxide Fuel Cell Forum, European Fuel Cell Forum, Oberrohfdorf, Switzerland (2002) 481–489.
[7] R. Mukundan, E.L. Brosha, F.H. Garzon, Electrochem. Solid-State Lett. 7 (2004) A5–A7.
[8] S. Jiang, S. Chan, Mater. Sci. Tech. 20 (2004) 1109–1118.
[9] T. Iida, M. Kawano, T. Matsui, R. Kikuchi, K. Eguchi, J. Electrochem. Soc. 154 (2007) B234–B241.
[10] D. Mogensen, J.D. Grunwaldt, P.V. Hendriksen, K. Dam-Johansen, J.U. Nielsen, J. Power Sources 196 (2011) 25–38.
[11] A.C. Gómez, R.R. Bustos, J. Van Duijn, Fuel Cells 11 (2011) 140–143.
[12] Y. Nabae, I. Yamanaka, Appl. Catal. A: Gen. 369 (2009) 119–124.
[13] S.I. Lee, K. Ahn, J.M. Vohs, R.J. Gorte, Electrochem. Solid-State Lett. 8 (2005) A48–A51.
[14] S. McIntosh, J.M. Vohs, R.J. Gorte, Electrochem. Solid-State Lett. 6 (2003) A240–A243.
[15] H. Sumi, K. Ukai, Y. Mizutani, H. Mori, C.J. Wen, H. Takahashi, O. Yamamoto, Solid State Ionics 174 (2004) 151–156.
[16] N. Lakshminarayanan, U.S. Ozkan, Appl. Catal. A: Gen. 393 (2011) 138–145.
[17] K. Sasaki, K. Susuki, A. Iyoshi, M. Uchimura, N. Imamura, H. Kusaba, Y. Teraoka, H. Fuchino, K. Tsujimoto, Y. Uchida, N. Jingo, J. Electrochem. Soc. 153 (2006) A2023–A2029.
[18] C.M. Grgicak, J.B. Giorgi, J. Phys. Chem. C 111 (2007) 15446–15455.
[19] M. Gong, X. Liu, J. Trembly, C. Johnson, J. Power Sources 168 (2007) 289–298.
[20] Y. Matsuzaki, I. Yasuda, Solid State Ionics 132 (2000) 261–269.
[21] H. He, R.J. Gorte, J.M. Vohs, Electrochem. Solid-State Lett. 8 (2005) A279–A280.
[22] Y.M. Choi, C. Compson, M.C. Lin, M. Liu, Chem. Physi. Lett. 421 (2006) 179–183.
[23] J.N. Kuhn, N. Lakshminarayanan, U.S. Ozkan, J. Mol. Catal. A: Chem. 282 (2008) 9–21.

[24] Z. Cheng, J.H. Wang, Y. Choi, L. Yang, M.C. Lin, M. Liu, Energy Environ. Sci. 4 (2011) 4380–4409.
[25] K. Haga, S. Adachi, Y. Shiratori, K. Itoh, K. Sasaki, Solid State Ionics 179 (2008) 1427–1431.
[26] S. Zha, P. Tsang, Z. Cheng, M. Liu, J. Solid State Chem. 178 (2005) 1844–1850.
[27] X.J. Chen, Q.L. Liu, S.H. Chan, N.P. Brandon, K.A. Khor, J. Electrochem. Soc. 154 (2007) B1206–B1210.
[28] A.L. Vincent, J.L. Luo, K.T. Chuang, A.R. Sanger, Appl. Catal. B: Environ. 160 (2011) 114–122.
[29] M. Roushanafshar, J.-L. Luo, A.L. Vincent, K.T. Chuang, A.R. Sanger, Int. J. Hydrogen Energy 37 (2012) 7762–7770.
[30] H. Kurokawa, L. Yang, C.P. Jacobson, L.C. De Jonghe, S.J. Visco, J. Power Sources 164 (2007) 510–518.
[31] L. Aguilar, S. Zha, S. Li, J. Winnick, M. Liu, Electrochem. Solid-State Lett. 7 (2004) A324–A326.
[32] O.A. Marina, L.R. Pederson, Proceedings of the 5th European Solid Oxide Fuel Cell Forum, in: J. Huijsmans (Ed.), Lucerne, Switzerland, 2002, p. 481.
[33] O.A. Marina, Presented at SECA Core Technology Program Review Meeting, Boston, MA (2004).
[34] O.A. Marina, N.L. Canfield, J.W. Stevenson, Solid State Ionics 149 (2002) 21–28.
[35] S. Tao, J.T.S. Irvine, Nat. Mater. 2 (2003) 320–323.
[36] L. Aguilar, S. Zha, Z. Cheng, J. Winnick, M. Liu, J. Power Sources 135 (2004) 17–24.
[37] P. Lohsoontorn, D. Brett, N. Brandon, J. Power Sources 175 (2008) 60–67.
[38] R.M. Ferrizz, R.J. Gorte, J.M. Vohs, Appl. Catal. B: Environ. 43 (2003) 273–280.
[39] D. Neagu, J.T.S. Irvine, Chem. Mater. 22 (2010) 5042–5053.
[40] M.E. Bowden, D.A. Jefferson, I.W.M. Brown, J. Solid State Chem. 117 (1995) 88–96.
[41] T. Ishihara, Bull. Chem. Soc. Jpn. 79 (2006) 1155–1166.
[42] Y. Chen, Y. Jiang, W. Li, R. Jin, S. Tang, W.H. Wenbin, Catal. Today 50 (1999) 39–47.
[43] O.A. Marina, M. Mogensen, Appl. Catal. A: Gen. 189 (1999) 117–126.
[44] X. Xu, F. Faglioni, W.A. Goddard, J. Phys. Chem. A 106 (2002) 7171–7176.
[45] J.A. Rodriguez, S. Chaturvedi, M. Kuhn, J. Hrbek, J. Phys. Chem. B 102 (1998) 5511–5519.
[46] E. Shustorovich, R.C. Baetzold, Science 227 (1985) 876–881.
[47] I.V. Yentekakis, C.G. Vayenas, J. Electrochem. Soc. 136 (1989) 996–1002.
[48] N. Laosiripojana, S. Assabumrungrat, Appl. Catal. B: Environ. 60 (2005) 107–116.
[49] E. Ramírez-Cabrera, A. Atkinson, D. Chadwick, Appl. Catal. B: Environ. 36 (2002) 193–206.
[50] Z. Wang, M. Flytzani-Stephanopoulos, Energy Fuels 19 (2005) 2089–2097.
[51] H.T. Chen, Y. Choi, M. Liu, M.C. Lin, J. Phys. Chem. C 111 (2007) 11117–11122.